



Cite this: *Phys. Chem. Chem. Phys.*,  
2018, 20, 6548

# Basic photophysical analysis of a thermally activated delayed fluorescence copper(i) complex in the solid state: theoretical estimations from a polarizable continuum model (PCM)-tuned range-separated density functional approach†

Lingling Lv,<sup>a</sup> Kun Yuan<sup>a</sup> and Yongcheng Wang<sup>b</sup>

A quantitative understanding of photophysical processes is fundamental for designing novel thermally activated delayed fluorescence (TADF) materials. Taking a Cu(pop)(pz<sub>2</sub>Bph<sub>2</sub>) crystal as a typical TADF molecular model, we computed the conversion and decay rates of the first excited singlet state (S<sub>1</sub>) and triplet state (T<sub>1</sub>) at different temperatures by employing the thermal vibration correlation function (TVCF) approach. For the consideration of the solid-state environment, a methodology, which is based on the combination of a nonempirical, optimally tuned range-separated hybrid functional with the polarizable continuum model, was applied. Our calculated results are in excellent agreement with the experimentally available data. It is found that the reverse intersystem crossing (RISC) from T<sub>1</sub> to S<sub>1</sub> proceeds at a rate of  $k_{\text{RISC}} = 6.34 \times 10^5 \text{ s}^{-1}$  and can compete with the radiative decay rate ( $k_r^T = 3.29 \times 10^3 \text{ s}^{-1}$ ) and nonradiative intersystem crossing rate ( $k_{\text{ISC}}^0 = 1.48 \times 10^2 \text{ s}^{-1}$ ) of T<sub>1</sub> at 300 K. This implies that the S<sub>1</sub> state can be repopulated from the T<sub>1</sub> state, TADF should be observed and the TADF decay time was found to be  $\tau$  (300 K) = 9.68  $\mu\text{s}$  by fitting calculations. In addition, the calculations indicate that the free rotation of the phenylene ring in the pop ligand can provide an important channel to energy conversion between T<sub>1</sub> and S<sub>1</sub>. But, at a low temperature of  $T < 100 \text{ K}$ , the situation will experience a larger change. The RISC rate becomes very small,  $k_{\text{RISC}} \ll k_r^T$  or  $k_{\text{ISC}}$ , and it cannot induce an occurrence of delayed fluorescence. As a consequence, Cu(pop)(pz<sub>2</sub>Bph<sub>2</sub>) is a highly attractive candidate for applications of TADF.

Received 10th December 2017,  
Accepted 29th January 2018

DOI: 10.1039/c7cp08264a

rsc.li/pccp

## Introduction

Recently, third-generation luminescent materials—thermally activated delayed fluorescence (TADF) molecules for organic light emitting diodes (OLEDs) have been extensively investigated because TADF allows the harvesting of both singlet and triplet excitons and the realization of internal quantum

efficiencies up to 100% when compared to those in phosphorescent OLEDs.<sup>1–4</sup> In an electroluminescence device, electrons and holes are electrically injected from electrodes to form excitons in the active layer. It is well known that exciton formation under electrical excitation typically results in 25% singlet excitons with only one ( $M_s = 0$ ) microstate and 75% triplet excitons with three spin angular projections ( $M_s = 0, \pm 1$ ). However, at ambient temperatures, about 75% of excitons are quenched by intramolecular vibrations and by phonons, which leads to the assumption that the fluorescence emission quantum yield has an upper statistical limit of 25% (Fig. 1).<sup>5–7</sup> To break through this bottleneck, more recently, one has found that TADF emitters can effectively convert the lowest triplet state (T<sub>1</sub>) into the lowest singlet state (S<sub>1</sub>) through reverse intersystem crossing (RISC) upon increasing the temperature, which largely improves the efficiency of the exciton utilization and even makes it reach 100% in principle.<sup>8–10</sup> Therefore, the research of TADF materials has become a hotspot for OLEDs.

Efficient TADF molecules have to simultaneously satisfy the conditions of a small energy splitting between the S<sub>1</sub> and T<sub>1</sub>

<sup>a</sup> College of Chemical Engineering and Technology, Tianshui Normal University, Tianshui, GanSu 741001, China. E-mail: lvling100@163.com

<sup>b</sup> College of Chemistry and Chemical Engineering, Northwest Normal University, Lanzhou, GanSu 730070, China. E-mail: ycwang02@163.com

† Electronic supplementary information (ESI) available: Vital structural parameters for Cu(pop)(pz<sub>2</sub>Bph<sub>2</sub>) using different functional methods; active transition orbitals of Cu(pop)(pz<sub>2</sub>Bph<sub>2</sub>) in the triplet state; Huang–Rhys factors and reorganization energies *versus* the normal modes in terms of the corresponding S<sub>0</sub> and S<sub>1</sub> potential surfaces at the PCM-tuned LC-BLYP\* level; the displacement vectors of three important vibration modes with the largest values of Huang–Rhys factor for the T<sub>1</sub> and S<sub>1</sub> states; the geometries are intuitive pictures comparing the S<sub>1</sub> and T<sub>1</sub> geometries at the PCM-tuned LC-BLYP\*/6-31 + G(d) level; cartesian coordinate of the PCM-tuned LC-BLYP\* optimized ground state and TD- LC-BLYP\* optimized excited state geometries. See DOI: 10.1039/c7cp08264a

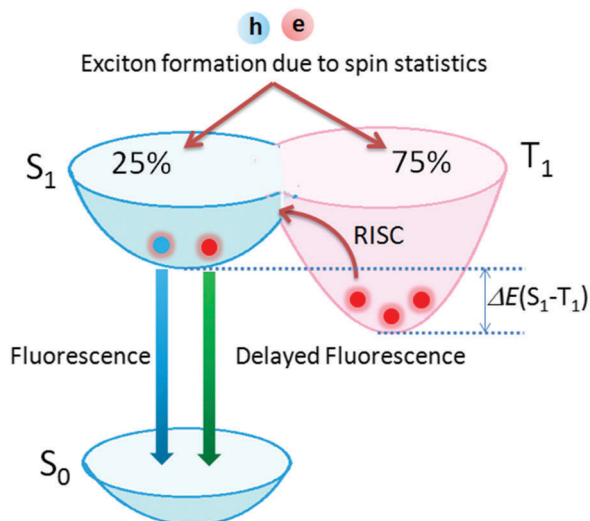


Fig. 1 Schematic diagram of the decayed fluorescence processes following exciton formation according to spin-statistics in TADF molecules.

states,  $\Delta E(S_1-T_1)$ , and minimise non-radiative decay to ensure that the  $T_1$  state lives long enough to maximise the chance of triplet harvesting through thermally activated RISC, see Fig. 1. Therefore, TADF molecules have often been designed following a strategy such that their highest occupied molecular orbital (HOMO) and lowest unoccupied molecular orbital (LUMO) are spatially separated to reduce their wave function overlap and lead to a small exchange energy, under the assumption that both  $S_1$  and  $T_1$  can be approximated by a one-electron transition from HOMO to LUMO.<sup>11</sup> However, in this simple model, one can obtain both  $\Delta E(S_1-T_1)$  and the radiative decay rate  $k_f^S$  of the  $S_1 \rightarrow S_0$  transition from integrals over the product of the HOMO and LUMO ("transition density").<sup>12</sup> A small transition density implies that both  $\Delta E(S_1-T_1)$  and  $k_f^S$  are small. Thus, the main challenge of the TADF molecular design is to strike the right balance and combine a small  $\Delta E(S_1-T_1)$  with a reasonable oscillator strength.

Very recently, TADF-type metal complexes came into the focus of research. In contrast to the previous phosphorescent OLEDs, Cu(i) complexes are well suited because their excited states often exhibit low-lying metal to ligand charge transfer (MLCT) states of  $^3\text{MLCT}$  and  $^1\text{MLCT}$  character.<sup>12,13</sup> They often have a much weaker SOC and the  $T_1 \rightarrow S_0$  transition is largely forbidden. At the same time, they generally have a small  $\Delta E(S_1-T_1)$  and a suitable transition dipole moment  $\mu(S_1 \rightarrow S_0)$ , which match two key features of the TADF mechanism.

Some efforts have been made to disclose the mechanism of photophysical processes in TADF-type Cu(i) complexes through experimental measurements and theoretical calculations.<sup>12–15</sup> However, a thorough understanding of photophysical processes is still scarce. For example, Yersin *et al.* found that large variations in the photoluminescence (PL) quantum yield and PL transient decay time of TADF guest molecules occur as a function of their environment in an experimental study;<sup>12</sup> Czerwieńiec *et al.* have reported that the same Cu(i) compound

can have a much higher PL quantum yield in the solid state than that in solution.<sup>14</sup> Marian *et al.* also reported the photophysical properties of a cationic three-coordinate Cu(i) complex with a monodentate N-heterocyclic carbene ligand and a bidentate phenanthroline ligand using the combined density functional theory and multireference configuration interaction method (DFT/MRCI),<sup>15</sup> but these authors did not discuss the solid state polarization effects, which can play a vital role in the determination of the nature of the excited states. In addition, we all know that the spin-orbit coupling (SOC) interaction can provide a major mechanism for a spin-forbidden ISC radiationless transition. But in most cases, SOC between the  $^3\text{MLCT}$  and  $^1\text{MLCT}$  of donor-acceptor Cu(i) complexes is forbidden (the same configuration). It is therefore unlikely for the interconversion processes of  $T_1 \rightarrow S_1$  to take place *via* RISC directly, especially in view of the large rate  $k_{\text{RISC}} \approx 10^7 \text{ s}^{-1}$  reported.<sup>16,17</sup> In this case, Ogiwara *et al.* proposed that RISC is driven by hyperfine coupling induced ISC.<sup>5</sup> However, the hyperfine coupling constants are very small, usually in the range of  $10^{-4} \text{ meV}$ , and this therefore also appears highly unlikely for the large rates.

As already discussed above, from a theoretical standpoint, the theoretical investigations of TADF molecules taking into account the solid state environment and thermal vibration activation are of course important but also challenging. In this study, we chose a typical Cu(i) complex TADF emitter, Cu(pop)(pz<sub>2</sub>Bph<sub>2</sub>), where pop = bis(2-(diphenylphosphanyl)-phenyl)ether and pz<sub>2</sub>Bph<sub>2</sub> = bis(pyrazol-1-yl)-diphenyl-borate (Fig. 2), as a model because it has a wealth of experimental photophysical and spectroscopic data.<sup>12,14</sup> For the consideration of the solid state environment, a methodology developed by Sun's group was applied,<sup>18</sup> and this method is based on the combination of an optimal tuning of the range-separation parameter  $\omega$  in a long-range corrected (LC) functional with the polarizable continuum model (PCM)-tuned approach, in which the solid-state screening effects are described *via* the consideration of the solid-state dielectric constant  $\epsilon$  in the context of the PCM approach (see Computational details). The interconversion and decay rate constants of  $S_1$  and  $T_1$  have been quantitatively calculated by employing the thermal vibration correlation function (TVCF) rate theory in combination with

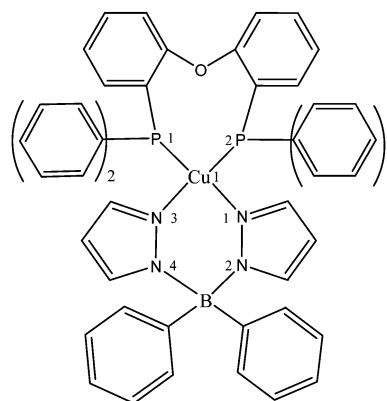


Fig. 2 Chemical structure of the mononuclear Cu(pop)(pz<sub>2</sub>Bph<sub>2</sub>) complex.

the PCM-tuned LC-BLYP\* method.<sup>19–22</sup> The absorption and emission spectra were obtained by the scalar relativistic LC-BLYP\* method combined with the restricted open-shell configuration interaction singles (ROCIS) method including spin-orbit coupling effects.<sup>23</sup> The motivation is to provide design routes for high-performance Cu(I) complex TADF materials.

## Computation details and theoretical background

### Geometry optimizations

The ground state geometries of the Cu(pop)(pz<sub>2</sub>Bph<sub>2</sub>) TADF molecule were initially optimized at the B3LYP/6-31+G(d) level of theory. As for the excited state optimizations, to seek a compromise between the computational cost and accuracy, the time-dependent density functional theory (TD-DFT) is a well-established tool to study the excited states of relatively large molecular systems. However, the TADF molecules mostly have a characteristic of large CT between the donor and acceptor units. TD-DFT calculations based on the standard functionals can severely underestimate the excitation energies when dealing with such large CT systems.<sup>24</sup> It has been shown that the errors mainly originate from the introduction of inappropriate exchange–correlation (XC) approximations and an incorrect behavior of the electron–electron potential at asymptotically large distances.<sup>25–27</sup> Recently, these shortcomings have been settled with the range-separated exchange (RS) density functional, in which the introduction of a suitable, fixed amount of exact-exchange (eX) has been shown to provide an improved description of the excited-state properties.<sup>28–30</sup> The general formula of the RS functionals can be expressed by the following eqn (1).<sup>31</sup>

$$\frac{1}{R_{12}} = \frac{1 - [\alpha + \beta \text{erf}(\omega R_{12})]}{R_{12}} + \frac{\alpha + \beta \text{erf}(\omega R_{12})}{R_{12}} \quad (1)$$

where the exchange term is divided into a long-range eX component derived from the Hartree–Fock equation and a short-range DFT component based on the error function (erf); the parameter  $\alpha$  quantifies the fraction of eX in the short-range limit, while  $\alpha + \beta$  gives the fraction of eX in the long-range limit. The range-separation parameter  $\omega$ , expressed in units of Bohr<sup>−1</sup>, represents the inverse of the distance  $R_{12}$  at which the exchange term switches from DFT to HF. The concept of “optimal tuning” corresponds to adjusting  $\omega$  to fulfill a fundamental property that the exact functional must obey in exact Kohn–Sham (KS) or generalized KS theory. In this work, the  $\omega$  tuning can be done according to eqn (2):<sup>18</sup>

$$J^2 = \sum_{i=0}^1 [\varepsilon_{\text{H}}(N+i) + \text{IP}(N+i)]^2 \quad (2)$$

here,  $\varepsilon_{\text{H}}$  and IP denote the corresponding HOMO energy and vertical ionization potential of the  $N + i$  electron systems, respectively.

For the solid state, we used the PCM-tuned RS functional approach, where the default integral equation formalism variant PCM was imported by adding the “scrf(pcm, solvent = generic,

read)” keyword.<sup>32</sup> Note that the term “crystal” simulated based on the presented model refers to the Cu(pop)(pz<sub>2</sub>Bph<sub>2</sub>) molecules in the crystalline phase compared to those in the gas phase. In addition, we also need to define the magnitude of the dielectric constant of the Cu(pop)(pz<sub>2</sub>Bph<sub>2</sub>) crystals. The dielectric constant  $\varepsilon$  was obtained *via* the Clausius–Mossotti eqn (3):<sup>33</sup>

$$\frac{\varepsilon - 1}{\varepsilon + 2} = \frac{4\pi \sigma}{3 V} \quad (3)$$

where  $\sigma$  denotes the isotropic component of the molecular polarizability;  $V$  represents the volume occupied by a single molecule calculated at the B3LYP/6-31+G(d) level.

According to the above methodology, the tuning optDFTw procedure based on the RS functionals (LC-BLYP and LC- $\omega$ PBE) with the 6-31+G(d) basis set is performed to determine the optimal  $\omega$  values when  $J^2$  reaches the minimum;<sup>18a,34,35</sup> henceforth, we denote the optimally-tuned RS functionals as LC-BLYP\* and LC- $\omega$ PBE\*, which were applied throughout this work. The ground geometries were then reoptimized using the new  $\omega$  values, for the sake of comparison, and the calculations were also performed with the widely used non-optimized CAM-B3LYP functional;<sup>31</sup> and the excited state structures were calculated using the time-dependent TD-LC-BLYP\* functional with the 6-31+G(d) basis set, followed by calculations of harmonic vibrational frequencies and normal modes to obtain equilibrium geometries and to calculate the thermal vibration correlation functions. All calculations were performed using the Gaussian 09 software.<sup>36</sup>

### Calculations of the excited-state properties

For the Cu(pop)(pz<sub>2</sub>Bph<sub>2</sub>) crystal molecule, electronic vertical absorption and emission were simulated with the parallel version of the combined PCM ( $\varepsilon = 3.82$ )-tuned LC-BLYP\* functional ( $\omega = 0.0475$  Bohr<sup>−1</sup>) and restricted open-shell configuration interaction with single excitations (DFT/ROCIS) method using version 4.0 of the ORCA package.<sup>37</sup> For the DFT/ROCIS calculations, the PCM-tuned LC-BLYP\* functional together with the parameters  $c_1 = 0.21$ ,  $c_2 = 0.49$ , and  $c_3 = 0.29$  was applied.<sup>23,38</sup> For all calculations, relativistic effects should be expected, which may have a significant effect on the calculated spectra. The resolution of the identity (RI) approximation was employed using the def2/J basis set combined with the scalar relativistically recontracted DKH-def2-TZVP(-f) basis set for the transition metal complexes.<sup>39</sup> Numerical integrations were done on a dense grid (ORCA grid5). The excitation energies and transition dipole moments for the spectrum including SOC were obtained with SOC-quasi-degenerate perturbation theory (QDPT).<sup>23</sup> Calculations with hybrid functionals were also performed using the RIJCOSX algorithm to speed up the calculation of the Hartree–Fock exchange.<sup>40</sup>

### Treatment of SOC and zero-field splitting

Spin and orbital angular momenta are coupled by the corresponding magnetic moment, which lifts the degeneracy resulting in a splitting of the spectrum. Many remarkable phenomena are associated with this splitting both in gaseous and condensed

phase material science. Such splitting of degeneracy occurs even in the absence of any external field, and accordingly, this splitting of the spectra is called zero-field splitting (ZFS).

ZFS contributions come from the classical spin-spin dipole interaction, along with the second-order SOC interaction, which introduces some angular momentum into the triplet state resulting in the ZFS spin parameters, axial  $D$  and rhombic  $E$ . The SOC calculation was performed on top of the above-mentioned PCM-tuned LC-BLYP\*/ROCIS calculations combined with the framework of QDPT. Herein, we employed an accurate multicenter spin-orbit mean-field (SOMF) of the Breit-Pauli SOC operator on all centers.<sup>41</sup>

In the SOMF method, we should note that the spin-same orbit and spin-other orbit contributions as well as the exchange effects are all treated to a good approximation. These calculations were performed with a key word of SOCFlags 1, 3, 3, 1 in the ORCA 4.0 program.<sup>37</sup> For comparison, SOC and the ZFS parameters are also calculated at the level of the complete active space self consistent field (CASSCF) wave function.

### Fluorescence and phosphorescence rate calculations

Intense fast fluorescence occurs from the singlet state (the  $S_1 \rightarrow S_0$  spin-allowed transition), whereas triplet transitions ( $T_1 \rightarrow S_0$ ) are strictly forbidden in the regime of an unrelativistic treatment. However, the forbidden emission can borrow dipole activity from the spin-allowed transitions ( $S_0 \leftrightarrow S_n$  and  $T_{1,\zeta} \leftrightarrow T_{m,\zeta}$ , see eqn (4)) through the perturbation of the SOC interactions, resulting in a nonzero intensity of transitions. The intensity of the transition is proportional to the square of the  $\mu(S_0 \leftarrow T_{1,\zeta})$  transition moment.  $\mu(S_0 \leftarrow T_{1,\zeta})$  can be written as follows:<sup>42,43</sup>

$$\begin{aligned} \mu(S_0 \leftarrow T_{1,\zeta}) &= \langle S_0 | \mu_z | T_{1,\zeta} \rangle \\ &= \sum_n \frac{\langle S_0 | \mu_z | S_n \rangle \langle S_n | \hat{H}_{\text{SOC}} | T_{1,\zeta} \rangle}{E(T_{1,\zeta}) - E(S_n)} \\ &\quad + \sum_m \frac{\langle T_{1,\zeta} | \mu_z | T_m \rangle \langle T_m | \hat{H}_{\text{SOC}} | S_0 \rangle}{E(T_m) - E(S_0)} \end{aligned} \quad (4)$$

where  $\zeta$  (= I, II, and III) represents one of the three SOC sublevels of the triplet  $T_{1,\zeta}$  state being subjected to the ZFS induced by the internal magnetic perturbations;  $\mu_z$  denotes an electric dipole moment operator projection on the  $z$  axis; and  $\hat{H}_{\text{SOC}}$  is the SOC operator. The corresponding calculations were performed with the PCM-tuned LC-BLYP\*/ROCIS method using the ORCA 4.0 program.<sup>37</sup> The electric transition dipole moments and vertical emission energies of the received spin-mixed wave functions can be used to calculate the rates according to eqn (5).<sup>42,43</sup>

$$k_{\tau,\zeta} = \frac{4e^2}{3c^3\hbar^4} \Delta E_{S_0 \leftarrow T_{1,\zeta}}^3 |\mu(S_0 \leftarrow T_{1,\zeta})|^2 \quad (5)$$

Where  $\Delta E_{S_0 \leftarrow T_{1,\zeta}}$  denotes a vertical emission energy.

$k_r$ , including the electronic-vibrational coupling by considering origin displacements, distortions, and Duschinsky rotation within a multimode harmonic oscillator model, is also obtained

by employing the TVCF method.<sup>19–22</sup> The  $k_r$  formalism can be expressed as the integration of eqn (6):<sup>20</sup>

$$\begin{aligned} \sigma(\omega, T) &= \frac{4e^2}{3c^3\hbar^4} |\mu(S_0 \leftarrow T_{1,\zeta})| \\ &\quad \times \int e^{-i\omega t} e^{i\omega S_0 - T_1} Z_i^{-1} \rho_{\text{em}}(t, T) dt \end{aligned} \quad (6)$$

$$k_r = \int_0^\infty \sigma_{\text{em}}(\omega) d\omega \quad (7)$$

where  $Z_{T_1}^{-1} = \sum_{v=\{0_1, 0_2, \dots, 0_N\}} e^{-\beta E_v^{T_1}}$  denotes the partition function,

and  $N$  is the number of normal modes;  $\rho_{\text{em}}(t, T) = \text{Tr}[e^{i\tau T_1} \hat{H}_{T_1} e^{i\tau S_0} \hat{H}_{S_0}]$  is defined as the TVCF form and can be solved analytically by multidimensional Gaussian integrations and their derivatives. Here,  $\tau_i = -i\beta - (t/\hbar)$ ,  $\tau_f = t/\hbar$ ,  $\beta = (k_B T)^{-1}$ , and  $\hat{H}_{T_1}(\hat{H}_{S_0})$  represent the harmonic oscillator-type Hamiltonians of the triplet (singlet) electronic state. These calculations were performed using the MOMAP program.<sup>19–22</sup>

### Calculations of intersystem crossing rates

Since the  $T_1$  and  $S_1$  states in the TADF Cu(I) complexes are of the same MLCT nature, there is almost no SOC-induced mixing between them. Therefore, the vibrational contributions to the ISC and RISC rates are especially important, and they are calculated with the TVCF method using the MOMAP program.<sup>19–22</sup> Thermal average ISC from the initial  $S_1$  electronic state with the vibrational quantum number  $u$  to the final  $T_1$  electronic state with the vibrational quantum number  $v$  may be expressed as eqn (8).<sup>21,44</sup>

$$\begin{aligned} k_{\text{ISC}} &= \frac{2\pi}{\hbar} |\langle T_1 | \hat{H}_{\text{SOC}} | S_1 \rangle|^2 Z_{T_1}^{-1} \\ &\quad \times \sum_{v,u} e^{-\beta E_v^{T_1}} |\langle \Theta_{T_1,v} | \Theta_{S_1,u} \rangle|^2 \delta(E_{T_1,v} - E_{S_1,u}) \end{aligned} \quad (8)$$

Here, the physical significance of the parameters is similar to eqn (9). The delta function  $\delta$  is used to keep the conservation of energy. Applying the Fourier transform of the  $\delta$  function, eqn (8) is rewritten as

$$k_{\text{ISC}} = \frac{1}{\hbar^2} |\langle T_1 | \hat{H}_{\text{SOC}} | S_1 \rangle|^2 \int_{-\infty}^{\infty} dt [e^{i\omega T_1, S_1} Z_{T_1}^{-1} \rho_{\text{ISC}}(t, T)] \quad (9)$$

in which the TVCF form is  $\rho_{\text{ISC}}(t, T) = \text{Tr}[e^{i\tau S_1} \hat{H}_{S_1} e^{i\tau T_1} \hat{H}_{T_1}]$ . The detailed derivations of these formulae are found in ref. 21. The ISC and RISC rates were calculated for six temperatures, from 30 K to 300 K. For integration of the time correlation function, a time interval of 0.1 fs and a grid of 65 536 points were chosen.

## Results and discussion

### Optimization of the range-separation parameter $\omega$ and the geometric structures

The tuning of the range-separation parameter  $\omega$  according to eqn (2) has been done for the LC-BLYP and LC- $\omega$ PBE



functionals using the tuning optDFTw procedure.<sup>34</sup> Fig. 3 plots the optimally tuned  $\omega$  values derived for the Cu(pop)(pz<sub>2</sub>Bph<sub>2</sub>) system in the gas, the solution (CH<sub>2</sub>Cl<sub>2</sub> solvent) and the solid phases. Compared to the default  $\omega = 0.47$  Bohr<sup>-1</sup> for the LC-BLYP functional and  $\omega = 0.40$  Bohr<sup>-1</sup> for the LC- $\omega$ PBE functional, the optimal  $\omega$  values significantly reduced to 0.1506 and 0.1566 Bohr<sup>-1</sup> for the gas phase system, respectively. The PCM model (CH<sub>2</sub>Cl<sub>2</sub> solvent) yields the very small optimal  $\omega = 0.0344$  Bohr<sup>-1</sup> (LC-BLYP\*) and 0.0374 Bohr<sup>-1</sup> (LC- $\omega$ PBE\*) due to the larger dielectric constants. Similar

optimal  $\omega$  values have been obtained for the solid state system, resulting in the values of 0.0475 and 0.0529 Bohr<sup>-1</sup> for LC-BLYP\* and LC- $\omega$ PBE\*, respectively. The tuned  $\omega$  value of a specific system can reflect the global delocalization degree, which is the inverse relationship between the tuned  $\omega$  value and the extent of global electron-delocalization. The smaller  $\omega$  values derived for the simulated solid environment are consistent with the expectation that the electron density is of a more delocalized nature in the solid environment than for an individual gas molecule. In addition, the parameter  $\omega$  reflects a characteristic

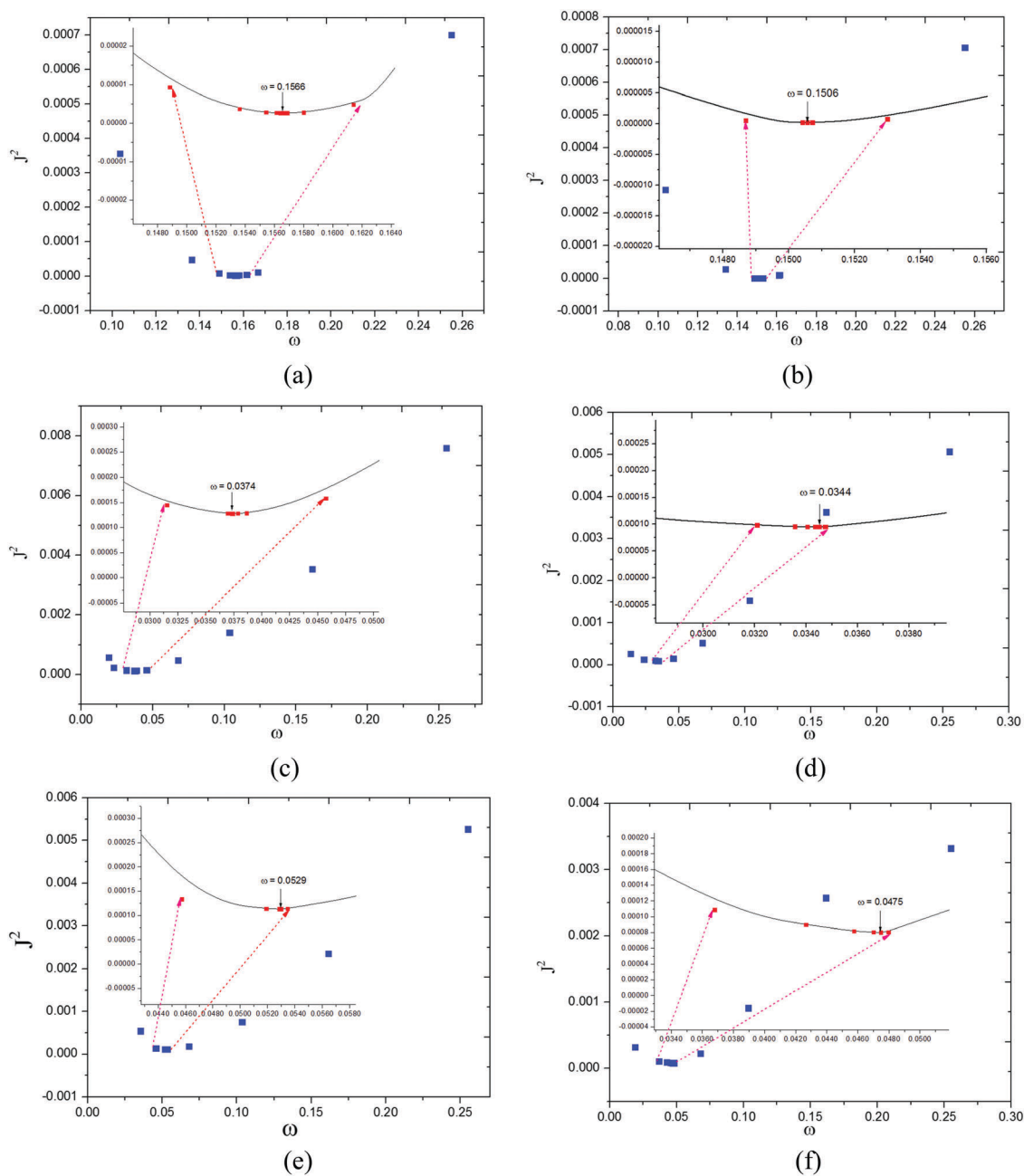


Fig. 3 Diagrams of error function  $J^2$  (a.u.) versus the range-separation parameter  $\omega$  (Bohr<sup>-1</sup>) calculated at the LC- $\omega$ PBE\*/6-31+G(d) level (a: gas state; c: solution state; e: solid state) and LC-BLYP\*/6-31+G(d) level (b: gas state; d: solution state; f: solid state). The optimal  $\omega$  values are printed in the corresponding boxes.

distance for switching between the short-range DFT-GGA (generalized gradient approximation) exchange and long-range eX since  $\omega$  corresponds to an inverse distance, in other words, such a small value of  $\omega$  implies that there is almost no long-range correction from the exact HF exchange.

In order to elucidate this behavior, Fig. 4 shows the relationship of the exact-exchange percentage (%HF) versus the inter-electronic distance ( $R_{12}$ ), where the different curves expressed the distinct behaviors of the tuned and original RS functionals. The results of the calculations performed using the conventional functionals are also plotted for the sake of comparison. Obviously, as the optimally tuned  $\omega$  values decrease, the curvature of the lines becomes smaller, compared with the corresponding original ones. Here, we take the tuned  $\omega$  value of the LC-BLYP\* functional for the Cu(pop)(pz<sub>2</sub>Bph<sub>2</sub>) system as an example. At  $R_{12} = 2.1$  a.u. for the gas phase, the optimally tuned functionals provide 32% ( $\omega = 0.1506$  Bohr<sup>-1</sup>) HF exchange, whereas LC-BLYP with a default value of 0.47 Bohr<sup>-1</sup> gives more than 82% HF exchange (Fig. 4a). When using the  $\omega$  value obtained for the Cu(pop)(pz<sub>2</sub>Bph<sub>2</sub>) solid state, the LC-BLYP\* functional includes only about 10% HF exchange and 90%

DFT-GGA exchange at  $R_{12} = 2.1$  atomic units. These results indicate that in order to accurately describe the polarization environment in the solid state, more DFT-GGA exchange and less HF exchange are required in the exchange functional. A lower fraction of HF exchange is really required to accurately predict the electron excitation energies and the more delocalized feature of the Cu(pop)(pz<sub>2</sub>Bph<sub>2</sub>) complex.

The geometric structures in the ground state ( $S_0$ ) of the Cu(pop)(pz<sub>2</sub>Bph<sub>2</sub>) complex in different environments were optimized using the optimally tuned functionals (LC- $\omega$ PBE\* and LC-BLYP\*) and conventional functionals (B3LYP and CAM-B3LYP). Fig. 5 displays the comparison of the structural parameters at the equilibrium geometries with the experimental values, and the mean absolute deviations (MADs) of the bond lengths and angles are inserted in the pictures. Detailed parameters of geometry are listed in Table S1 in the ESI.† It is easily seen that the geometric structure of  $S_0$  is most sensitive to the choice of functionals. Based on the MAD values of the geometric parameters, the calculated results of the B3LYP and CAM-B3LYP functionals show larger deviations (*i.e.* MADs of 0.0085 and 0.0568 Å for the bond lengths, respectively; 2.18 and 2.21° for the bond angles) compared with the crystal data in the solid environment. However, the optimally tuned RS functionals (LC-BLYP\* and LC- $\omega$ \*PBE) with the greatly decreased MADs reveal their outstanding performance in predicting the structure for a CT-type molecule. A similar situation is also observed in the gas phase and in solution, especially for the PCM-tuned ( $\omega = 0.0475$  Bohr<sup>-1</sup>) LC-BLYP\* functional where the MADs were merely 0.0274 Å for the bond lengths and 1.95° for the bond angles. Thus, considering the advantages of the optimally tuned RS functionals, we ultimately chose the PCM-tuned ( $\omega = 0.0475$  Bohr<sup>-1</sup>) LC-BLYP\* level, unless otherwise stated, to calculate the geometric structures (including the  $S_0$ ,  $S_1$  and  $T_1$  states) and the electron excitation properties of the Cu(pop)(pz<sub>2</sub>Bph<sub>2</sub>) crystal. We used the Cu(pop)(pz<sub>2</sub>Bph<sub>2</sub>) crystal as a workhorse model as there is sufficient experimental evidence to enable comparison with the theoretical results.

### Excited-state properties and singlet–triplet splitting $\Delta E(S_1-T_1)$

In Fig. 6, a comparison between the experimental spectrum of the Cu(pop)(pz<sub>2</sub>Bph<sub>2</sub>) crystal and the simulated result obtained at the PCM-tuned LC-BLYP\*/ROCIS functional level without and with SOC effects is reported. The experimental absorption spectrum shows a weak band at 370 nm, which was assigned to the CT  $S_0 \rightarrow S_1$  transition involving the 3d metal orbitals and pop ligand-centered  $\pi^*$ -orbital.<sup>14</sup> The simulated and experimental spectra are seen to match perfectly from Fig. 6, with the simulated spectrum of 371.7 nm for the  $S_0 \rightarrow S_1$  transition. The calculations show that the  $S_1$  main configuration originates from the MLCT transition from the HOMO to the LUMO, and a molecular orbital scheme with graphical representations of the Kohn–Sham orbital densities is shown in Fig. 7. The HOMO has d character originating from a linear combination of the d orbital of the Cu(I) atom with p orbitals of the coordinating phosphorous atoms, whereas the LUMO is mainly distributed

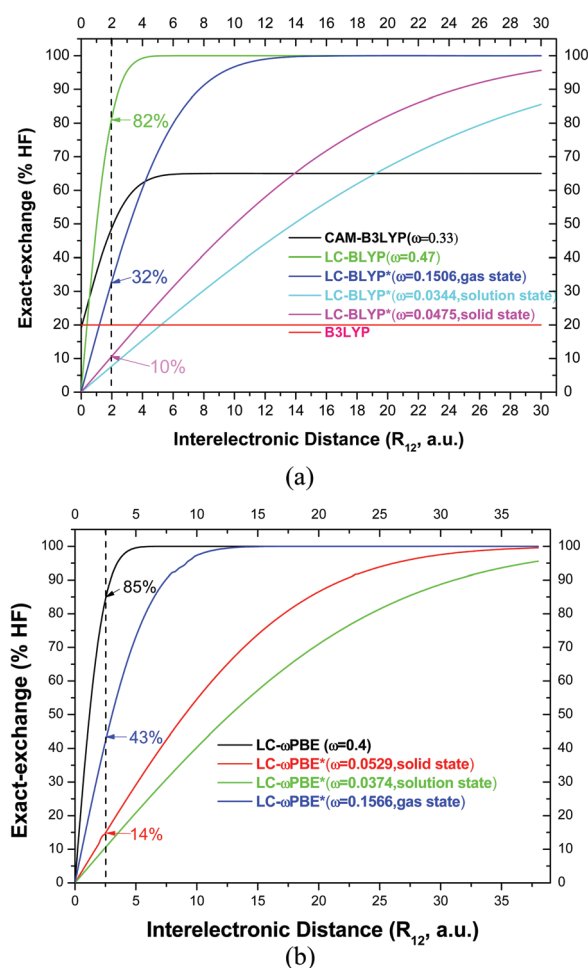


Fig. 4 Percentage of the exact-exchange (%HF) included as a function of the interelectronic distance ( $R_{12}$ ) for the LC- $\omega$ PBE functional (a) and the B3LYP, CAM-B3LYP, and LC-BLYP functionals (b).

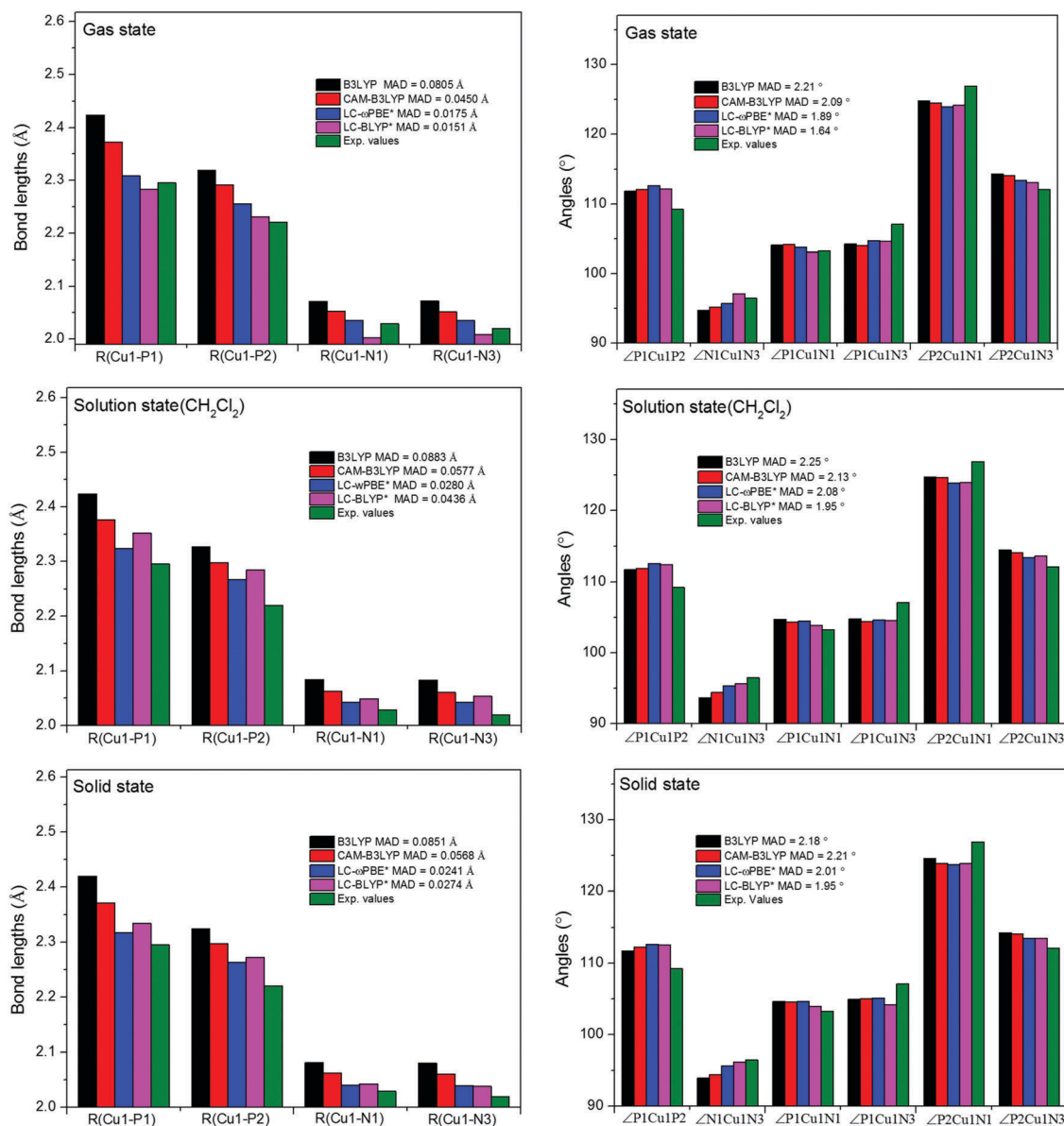


Fig. 5 Calculated vital geometric parameters (bond lengths and angles) at the equilibrium geometries of the ground state  $S_0$  for the Cu(pop)(pz<sub>2</sub>Bph<sub>2</sub>) TADF molecule using different density functions in the gas, solution and solid states compared to the experimental values. MAD: mean absolute deviation of the bond lengths and angles are inserted in the pictures, and the MAD values are calculated with respect to the corresponding experimental values, e.g.  $MAD = 1/n \sum |R_{cal.} - R_{exp.}|$ .

over the phenylene ring of the pop ligand. This reveals a special excited state formation, that is, the MLCT process with charge transfer from the metal to an empty antibonding  $\pi^*$  orbital of the pop ligand.

Upon inclusion of SOC, we find that the  $S_1$  absorption spectrum at 371.9 nm is only slightly red-shifted and reduced in intensity with respect to the one without SOC, but it essentially preserves its singlet-singlet MLCT character. Vital differences can be seen in the line spectrum (377.7 nm), where the excitation gains oscillator strength due to the  $S_0 \rightarrow T_1$  interaction. In principle, the SOC perturbed states borrow their intensities from those of the singlet-singlet allowed

states (see eqn (7)). Based on eqn (7), the two terms have an inverse dependence on the energy differences between the spin manifolds. Since the energy splitting between  $S_0$  and  $T_m$  is much greater than the energy splitting between  $T_1$  and  $S_m$ , the intensity of the second term is much less than the first term (as is the  $n = 0$  element of the first term). In this way, the  $T_1$  state couples with the excited singlet states,  $S_m$ , mixing in contributions from the electric-dipole allowed excitations in the singlet  $S_0 \leftrightarrow S_m$  manifold. Thus, the formally spin forbidden  $S_0 \rightarrow T_m$  excitation is activated *via* SOC interaction. For the PCM-tuned LC-BLYP\*/ROCIS method, at 377.7 nm (26472  $\text{cm}^{-1}$ ), there is an excitation with substantial oscillator strength that has no

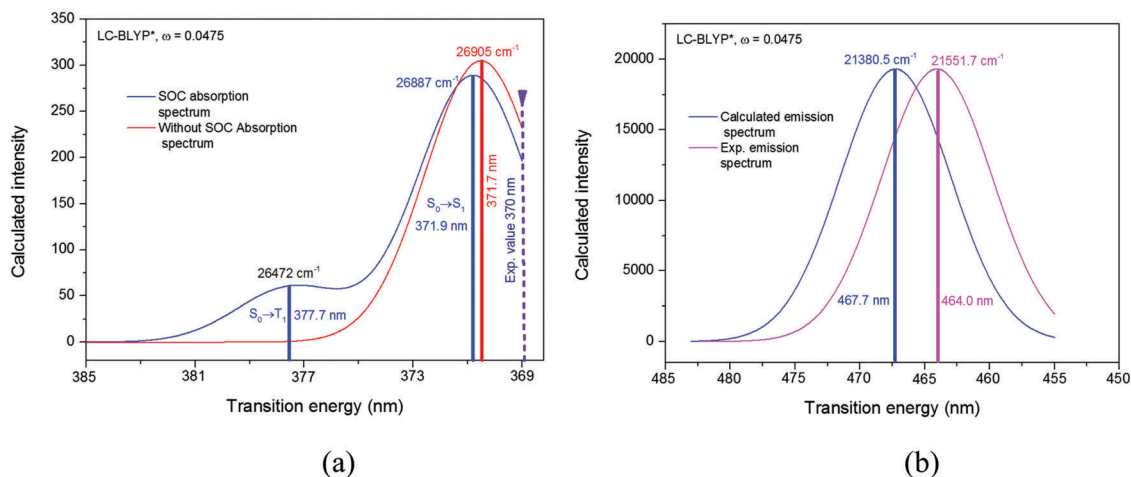


Fig. 6 Absorption spectra obtained at the scalar relativistic PCM-tuned LC-BLYP\*/ROCIS level including the SOC effects by means of QDPT (a); and the scalar relativistic PCM-tuned LC-BLYP\*/ROCIS emission spectrum (b). The data of the experimental spectrum were taken from Fig. 5 of ref. 14.

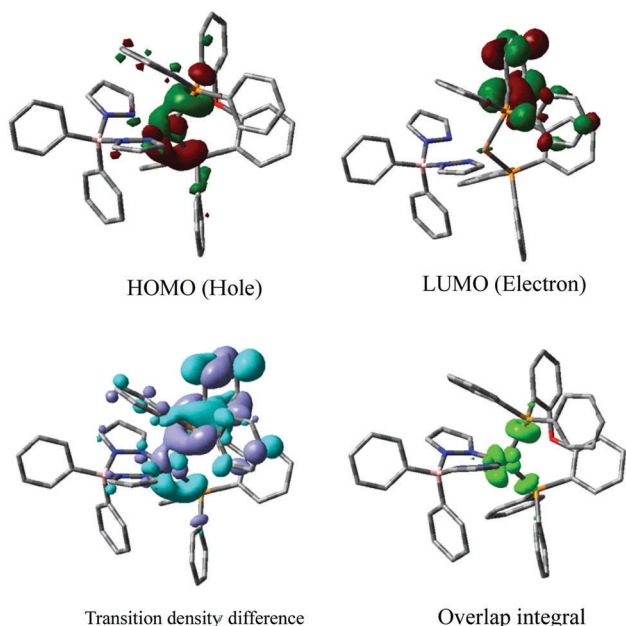


Fig. 7 HOMO and LUMO of Cu(pop)(pz<sub>2</sub>Bph<sub>2</sub>) displayed in the solid state, as calculated at the PCM-tuned LC-BLYP\*/6-31+G(d) level. Hydrogen atoms are omitted for clarity. The transition density difference between the HOMO and LUMO and the overlap integral are displayed in the lower part of the diagram.

correspondence with the spin-free spectrum. It is a  $S_0 \rightarrow T_1$  excitation with some singlet excited state admixture, and the  $T_1$  state also has the character of the MLCT excitation compared to the  $S_1$  state.

The emission spectrum of the Cu(pop)(pz<sub>2</sub>Bph<sub>2</sub>) crystal is in accordance with the MLCT nature of the emitting state, and the emission maxima is found at a  $\lambda_{\text{max}}$  value of 464 nm for the neat sample. The experimental result is in agreement with the calculated value of 467.7 nm for the  $S_1$  structure in the crystalline environment.<sup>14</sup> These observations also show that the PCM-tuned LC-BLYP\*/ROCIS method can simulate the

excited properties of the Cu(pop)(pz<sub>2</sub>Bph<sub>2</sub>) crystal in the solid state well.

For the TADF molecules, RISC depends on the energy splitting  $\Delta E(S_1-T_1)$  between  $S_1$  and  $T_1$ , and it should be as small as possible. As already discussed above, the  $S_1$  and  $T_1$  states have the same configurations, <sup>1</sup>MLCT and <sup>3</sup>MLCT, from the  $d \rightarrow \pi^*$  MLCT excitations. In this situation,  $\Delta E(S_1-T_1)$  is well approximated by twice the exchange integral for HOMO and LUMO. The exchange integral can be interpreted as the electrostatic interaction of the transition density  $\rho_{\text{H,L}} = \text{HOMO-LUMO}$  with itself. A reason for the small transition density is depicted schematically in Fig. 7 as a “small overlap” of the HOMO and LUMO. We choose the PCM-tuned LC-BLYP\*/ROCIS approach to evaluate  $\Delta E(S_1-T_1)$  at the def2-TZVP(-f) basis set level in the crystalline environment. Compared to the experimental value of  $\Delta E(S_1-T_1) = 800 \text{ cm}^{-1}$ ,<sup>14</sup> it is apparent that the PCM-tuned LC-BLYP\*/ROCIS ( $737.2 \text{ cm}^{-1}$ , see Table 1) method gives the best prediction of  $\Delta E(S_1-T_1)$  at the  $T_1$  geometry.

### Phosphorescence and fluorescence

In order to achieve a deeper photophysical understanding of TADF materials, a detailed study of the  $T_1$  state is vital. A triplet state consists of three substates due to anisotropic spin dipolar interactions and SOC, even in the zero field, which can cause these substates to have quite different radiative and nonradiative properties. Yersin and co-workers have experimentally determined the ZFS values of the order of 1 to  $10 \text{ cm}^{-1}$  for the Cu(pop)(pz<sub>2</sub>Bph<sub>2</sub>) crystal.<sup>12,14</sup> Our PCM-tuned LC-BLYP\*/ROCIS result shows that  $\Delta E_{\text{I,II}} = 0.4 \text{ cm}^{-1}$  and  $\Delta E_{\text{II,III}} \approx 3 \text{ cm}^{-1}$ , in good agreement with the experimental results (see Table 1). For the sake of comparison, the computed values of  $D = 3.19 \text{ cm}^{-1}$  and  $E = 0.22 \text{ cm}^{-1}$  ( $\Delta E_{\text{I,II}} = E$ ;  $\Delta E_{\text{II,III}} = D$ ) using the CASSCF method at the  $T_1$  geometry, and the corresponding vital SOC values between  $T_1$  and  $S_n$  or  $T_m$  are all given in Table 2 at the CASSCF(10,8)/def2-TZVP(-f) level, and the space active orbitals are shown in Fig. S1 (ESI<sup>†</sup>).



**Table 1** Vertical transition energies  $\Delta E$ , oscillator strength  $f$ , radiative rates  $k_r$ , and lifetimes  $\tau$  at the  $T_1$  minimum at the PCM-tuned LC-BLYP\*/ROClS/def2-TZVP(-f) levels and the corresponding experimental values are listed in the table

State	$\Delta E$ (cm <sup>-1</sup> )	$F$	$k_r$ (s <sup>-1</sup> )	$\tau$ ( $\mu$ s)
Solid state				
$T_{1,I}$	20643.3	$4.07 \times 10^{-6}$	$1.16 \times 10^3$	862
$T_{1,II}$	20643.7	$1.58 \times 10^{-5}$	$4.49 \times 10^3$	223
$T_{1,III}$	20646.3	$1.40 \times 10^{-6}$	$3.98 \times 10^2$	2513
Average			$k_{p,av} = 2.02 \times 10^3$	$\tau_{av}(T_1) = 495$
$S_1$	21380.5	$3.44 \times 10^{-2}$	$1.05 \times 10^7$	0.095
$\Delta E(S_1-T_1)$	737.2			
Exp. values	$\Delta E(S_1-T_1) = 800$		$k_{p,av} = 2.0 \times 10^3$	$\tau_{av}(T_1) = 480, \tau_I = 600, \tau_{II} = 170, \tau_{III} = 2000, \tau(S_1) = 0.12$

**Table 2** calculated spin-orbit coupling matrix constants (SOCC) (cm<sup>-1</sup>) between  $T_1$  and  $S_n$  or  $T_m$  for the mononuclear Cu(pop)(pz2Bph2) complex and the tensors  $D$  and  $E$  of ZFS with units in cm<sup>-1</sup> at the CASSCF(8,7)/def2-TZVP(f) level

States		$\langle T_1   \hat{H}_{SOC}   S_n \rangle$ or $\langle T_1   \hat{H}_{SOC}   T_m \rangle$			SOCC <sup>a</sup>	ZFS	
		$x$	$y$	$z$		$D$	$E$
$T_1$	$S_1$	-1.18	-1.16	-7.11	4.20	3.19	0.22
	$S_2$	-381.53	53.59	-48.70	224.20		
	$S_3$	-361.87	388.19	327.30	359.98		
	$S_4$	8.23	0.18	1.97	4.89		
	$S_5$	6.68	2.18	-1.13	4.11		
	$T_1$	0.00	0.00	0.00	0.00		
	$T_2$	-536.86	71.35	-70.93	315.35		
	$T_3$	515.34	-549.62	-462.19	510.32		
	$T_4$	1.94	-1.88	2.02	1.95		
	$T_5$	0.29	0.13	0.40	0.29		

$$^a \text{SOCC} = \sqrt{\left( |\langle T_1 | \hat{H}_{SOC} | S_n \rangle_x|^2 + |\langle T_1 | \hat{H}_{SOC} | S_n \rangle_y|^2 + |\langle T_1 | \hat{H}_{SOC} | S_n \rangle_z|^2 \right) / 3}.$$

It is well known that ZFS is determined by two contributions from the spin-spin dipolar interactions and the SOC interactions. The shift in the sublevel energy mainly originates from a singlet-triplet ( $E_{\zeta}^{ST}$ ) SOC and a triplet ( $E_{\zeta}^{TT}$ ) SOC for the heavy-metal compounds, which are expressed as eqn (10a) and (10b), respectively:<sup>45</sup>

$$E_{\zeta}^{ST} = \sum_n \frac{|\langle T_{1,\zeta}(^3d\pi^*) | \hat{H}_{SOC} | S_n(^1d'\pi^*) \rangle|^2}{E(S_n) - E(T_{1,\zeta})}, \quad \zeta = \text{I, II, III} \quad (10a)$$

$$E_{\zeta}^{TT} = \sum_m \frac{|\langle T_{1,\zeta}(^3d\pi^*) | \hat{H}_{SOC} | T_{m,\zeta}(^1d'\pi^*) \rangle|^2}{E(T_{m,\zeta}) - E(T_{1,\zeta})}, \quad \zeta = \text{I, II, III} \quad (10b)$$

On the basis of eqn (10a), the contribution of the SOC between  $T_1$  and  $S_1$  on the ZFS is almost zero because the  $S_1$  and  $T_1$  states have the same configurations,  $^1,^3d\pi^*$ , which lead to the forbidden coupling. It is well known that the SOC matrix element can be written in terms of ladder operators (eqn (11)).<sup>4</sup>

$$\begin{aligned} \langle \phi_1 | \hat{h}_{SOC}(\mathbf{A}) | \phi_2 \rangle &= \xi(\mathbf{A}) \langle \chi_1 | l(\mathbf{A}) | \chi_2 \rangle \cdot \langle \theta_1 | s | \theta_2 \rangle \\ &= \xi(\mathbf{A}) [\langle \chi_1 | l_z(\mathbf{A}) | \chi_2 \rangle \cdot \langle \theta_1 | s_z | \theta_2 \rangle \\ &\quad + 0.5 \langle \chi_1 | l_+(\mathbf{A}) | \chi_2 \rangle \cdot \langle \theta_1 | s_- | \theta_2 \rangle \\ &\quad + 0.5 \langle \chi_1 | l_-(\mathbf{A}) | \chi_2 \rangle \cdot \langle \theta_1 | s_+ | \theta_2 \rangle] \\ \sum_i \hat{h}_{SOC}(\mathbf{A}) &= \hat{H}_{SOC} \quad \phi = \chi \cdot \theta \text{ with } \theta = \uparrow, \downarrow \end{aligned} \quad (11)$$

where  $l$  and  $s$  denote the orbital and spin angular momentum operators, respectively; spin-orbitals  $\phi$  can be written as the products of spatial orbitals  $\chi$  times spin parts  $\theta$ ; the arrows  $\uparrow$  and  $\downarrow$  represent the traditionally used spin notations  $\alpha$  and  $\beta$ , respectively. The  $l_+s_-$  or  $l_-s_+$  operator in eqn (11) performs a spin-flip and this process is accompanied by a change in the orbital due to the  $l_+/l_-$  raising/lowering operator. For the  $T_1$  and  $S_1$  states, the matrix element  $\langle T_1(^3d\pi^*) | \hat{H}_{SOC} | S_1(^1d\pi^*) \rangle$  can be expressed by a sum of

$$\langle \pi^* \downarrow | \hat{h}_{SOC} | \pi^* \uparrow \rangle = \xi(\mathbf{A})/2 \langle \pi^* | l_{\pm}(\mathbf{A}) | \pi^* \rangle \langle \downarrow | s | \uparrow \rangle$$

and

$$\langle d \downarrow | \hat{h}_{SOC} | d \uparrow \rangle = \xi(\mathbf{A})/2 \langle d | l_{\pm}(\mathbf{A}) | d \rangle \langle \downarrow | s | \uparrow \rangle$$

Two orbitals of opposite spins in SOC have to be different spatial components, but for the triplet state  $T_1$ , its wave function cannot meet this rule: i.e., the two orbitals of opposite spins in the SOC interaction have the same spatial orbits. SOC between a  $S_1(^1d\pi^*)$  state and a  $T_1(^3d\pi^*)$  substate involving the same d-orbital can be neglected. This analysis is very consistent with the small values calculated to be ( $\langle \phi_1 | \hat{h}_{SOC,x} | \phi_3 \rangle = -1.18$ ,  $\langle \phi_1 | \hat{h}_{SOC,y} | \phi_3 \rangle = -1.16$ , and  $\langle \phi_1 | \hat{h}_{SOC,z} | \phi_3 \rangle = -7.11$  cm<sup>-1</sup>, see Table 2).

In addition, we note that the SOC interactions between the other higher excited states  $S_n$  ( $n = 2$ , and 3) and  $T_1$  are very strong (Table 3). Since both orbitals d and d' are situated at the

**Table 3** Excited state decay rate constants obtained by the PCM-tuned LC-BLYP\* calculations at different temperatures including the thermal vibration activation (in units of  $s^{-1}$ ) for the Cu(pop)(pz<sub>2</sub>Bph<sub>2</sub>) powder

Temperature (K)	$k_F^S$	$k_{nr}^S$	$k_{ISC}$	$k_{RISC}$	$k_T^T$	$k_{ISC}^0$ <sup>a</sup>
30	$1.22 \times 10^7$	$2.88 \times 10^{10}$	$1.98 \times 10^0$	$8.59 \times 10^{-3}$	$3.52 \times 10^3$	
50	$1.22 \times 10^7$	$2.80 \times 10^{10}$	$1.55 \times 10^2$	$1.47 \times 10^{-2}$	$3.52 \times 10^3$	
80	$1.21 \times 10^7$	$9.73 \times 10^9$	$1.38 \times 10^4$	$9.62 \times 10^0$	$3.50 \times 10^3$	
100	$1.21 \times 10^7$	$2.51 \times 10^9$	$9.42 \times 10^4$	$2.40 \times 10^2$	$3.49 \times 10^3$	
200	$1.18 \times 10^7$	$1.80 \times 10^7$	$7.88 \times 10^6$	$2.43 \times 10^5$	$3.40 \times 10^3$	
300	$1.14 \times 10^7$	$3.01 \times 10^3$	$9.45 \times 10^6$	$6.34 \times 10^5$	$3.29 \times 10^3$	$1.48 \times 10^2$

<sup>a</sup> Rates of intersystem crossing  $k_{ISC}^0$  tend to be infinitesimal between 30 K and 200 K.

central metal Cu(I), their spin-orbit coupling is significant ( $\xi(\text{Cu}) = 857 \text{ cm}^{-1}$ ). Hence, the coupling between the corresponding substates can be large, but the contributions of ZFS are neglected due to the larger energy denominators. Thus, a correspondingly small energy splitting in the  $T_1$  state mainly originates from the SOC-induced weak mixing of the higher-lying triplet MLCT states with the lowest  $T_1$  substates ( $T_{1I}$ ,  $T_{1II}$ , and  $T_{1III}$ ).

With respect to ZFS, the phosphorescence and fluorescence rates or lifetimes have been calculated using the Einstein spontaneous emission formula, respectively, in the solid phase, and are listed in Table 1. At the  $T_1$  geometry, we found that the phosphorescence radiative rates of the three substates are  $k_{P,I} = 1.16 \times 10^3 \text{ s}^{-1}$  ( $\tau_I = 862 \mu\text{s}$ ),  $k_{P,II} = 4.49 \times 10^3 \text{ s}^{-1}$  ( $\tau_{II} = 223 \mu\text{s}$ ), and  $k_{P,III} = 3.98 \times 10^2 \text{ s}^{-1}$  ( $\tau_{III} = 2513 \mu\text{s}$ ), respectively, which are in reasonable agreement with the experimentally measured values (which are  $\tau_I = 600 \mu\text{s}$ ,  $\tau_{II} = 170 \mu\text{s}$ , and  $\tau_{III} = 2000 \mu\text{s}$ ).<sup>14</sup> For such small energy separations between the  $T_1$  sublevels, these experimental values were observed at a low temperature due to the very slow spin-lattice relaxation (SLR) processes. With an increase in the temperature, however, the SLR processes become significantly faster resulting in a fast thermalization of the three substates, and the averaged emission decay time  $\tau_{av}$  of the three substates can be calculated by the three individual decay times according to  $\tau_{av} = 3(\tau_I^{-1} + \tau_{II}^{-1} + \tau_{III}^{-1})^{-1}$  ( $\tau_I$ ,  $\tau_{II}$ , and  $\tau_{III}$  represent the emission decay times of the  $T_{1I}$ ,  $T_{1II}$ , and  $T_{1III}$  substates).<sup>43</sup> From Table 1 and Fig. 8, it can be observed that the calculated mean for the three phosphorescence rates is  $k_{P,av} = 2.02 \times 10^2 \text{ s}^{-1}$  ( $\tau_{av} = 495 \mu\text{s}$ ), and the rate for the fluorescence is  $k_F = 1.05 \times 10^7 \text{ s}^{-1}$  ( $\tau_F = 0.095 \mu\text{s}$ ), which are in good agreement with the experimentally measured values of  $\tau_{av} = 480 \mu\text{s}$  and  $\tau_F = 0.12 \mu\text{s}$ .<sup>14</sup>

### TADF and RISC

As discussed above, the photophysical properties of the TADF molecules are very sensitive to temperature. The emission properties are obtained by calculating the decay time as a function of temperature in the range from 10 to 300 K, using the formula fitted by many experimentalists, eqn (12),<sup>46</sup> and these results are plotted in Fig. 9.

$$\tau(T) = \frac{3 + \exp[-\Delta E(S_1 - T_1)/k_B T]}{\frac{3}{\tau(T_1)} + \frac{1}{\tau(S_1)} \exp[-\Delta E(S_1 - T_1)/k_B T]} \quad (12)$$

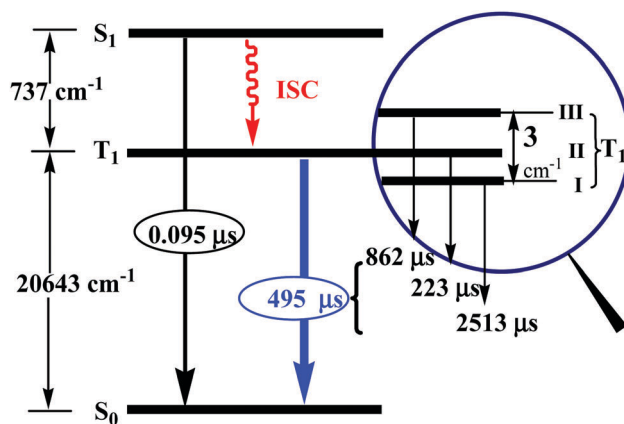


**Fig. 8** The energy separations including ZFS of the excited states and time constants of the transitions between the excited states and the ground state for the mononuclear Cu(pop)(pz<sub>2</sub>Bph<sub>2</sub>) complex in the solid state, as calculated at the PCM-tuned LC-BLYP\*/ROCIS/def2-TZVP(-f) level.  $\tau(T_1) = 495 \mu\text{s}$  represents the average decay time of the three sublevels of the triplet state  $T_1$ .

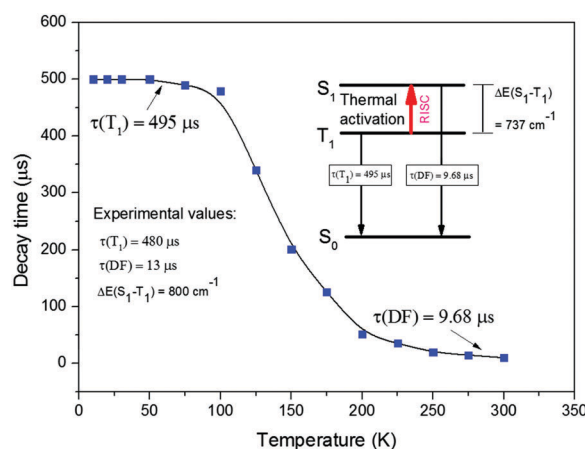


**Fig. 9** Emission decay time of the mononuclear Cu(pop)(pz<sub>2</sub>Bph<sub>2</sub>) complex versus temperature from 10 K to 300 K calculated from a fit procedure using eqn (12). Corresponding experimental values are inserted in the left part.

where  $k_B$  is the Boltzmann constant, and  $\tau(T_1)$  and  $\tau(S_1)$  are the intrinsic decay times of the emitting  $T_1$  and  $S_1$  states, respectively, in the absence of thermalization. One should note that eqn (12) has a limitation at very low temperatures due to the disappearance of the exponential terms. But at ambient

temperatures, a fast thermalization between the two excited states occurs, and eqn (12) can be well applied. From Fig. 9, for the Cu(pop)(pz<sub>2</sub>Bph<sub>2</sub>) crystal, at  $T < 100$  K, the emission decay time is almost constant and one observes a plateau at  $\tau(T_1) \approx 495$   $\mu$ s. This emission is assigned to phosphorescence from the triplet  $T_1$  to the ground state  $S_0$ . With increasing temperature, a sharp reduction is observed in the decay time. At temperatures above  $T \approx 250$  K, the contribution of the  $S_1$  state to the emission dominates, and the emission decay time of  $\tau(\text{DF}) \approx 9.68$   $\mu$ s represents the  $S_1 \rightarrow S_0$  fluorescence because it is fed by the long lived triplet state reservoir, which shows a delayed fluorescence. Fortunately, the value of  $\tau(\text{DF}) = 9.68$   $\mu$ s at  $T = 300$  K obtained by fitting eqn (12) is very close to the experimental value of 13  $\mu$ s.<sup>14</sup>

However, we know that TADF can effectively take place, through the RISC process. Thus, it is crucial to understand the RISC mechanism of the interconversion processes of  $T_1 \leftrightarrow S_1$ . To actually take place, the  $S_1$  state has to be repopulated with a temperature increase. This signifies that the RISC rate ought to be larger than the rates of the radiative and nonradiative decay of the  $T_1$  state to the ground state. Since the  $S_1$  and  $T_1$  states have the same configurations and almost the equivalent weights, their mutual SOC interaction is fairly weak (detailed discussion in Section 3.4), and the vibronic effects may have to be taken into account.

Here, the ISC and RISC rates including the vibrational contributions were computed according to eqn (8) and (9) using the MOMAP program. RISC proceeds at a rate of  $k_{\text{RISC}} = 6.34 \times 10^5$   $\text{s}^{-1}$  at 300 K, which is 2 orders of magnitude larger than the mean phosphorescence rate,  $k_{\text{T}}^{\text{T}} = 3.29 \times 10^3$   $\text{s}^{-1}$  (see Fig. 10), at the same time,  $k_{\text{RISC}}$  is 3 orders of magnitude larger than the ISC rate of  $k_{\text{ISC}}^0 = 1.48 \times 10^2$   $\text{s}^{-1}$  from  $T_1$  to  $S_0$ . This means that the  $S_1$  state can be populated from the  $T_1$  state. In addition, the ISC rate  $k_{\text{ISC}} = 0.945 \times 10^7$   $\text{s}^{-1}$  is again very close to the fluorescence rate  $k_{\text{T}}^{\text{S}} = 1.14 \times 10^7$   $\text{s}^{-1}$ . Therefore, under the conditions of  $k_{\text{ISC}} > k_{\text{T}}^{\text{S}} + k_{\text{nr}}^{\text{S}}$  and  $k_{\text{RISC}} > k_{\text{T}}^{\text{T}} + k_{\text{ISC}}^0$ , we conclude that the  $S_1$  and  $T_1$  state populations rapidly equilibrate before decaying radiatively at room temperature. The delayed

fluorescence occurs. Corresponding to the prompt and delayed fluorescence quantum efficiency,  $\Phi_{\text{p}}$  and  $\Phi_{\text{d}}$  (eqn (13)) are calculated, respectively, at 300 K.<sup>47</sup>

$$\Phi_{\text{p}} = \frac{k_{\text{T}}^{\text{S}}}{k_{\text{T}}^{\text{S}} + k_{\text{nr}}^{\text{S}} + k_{\text{ISC}}} \text{ and } \Phi_{\text{d}} = \sum_{m=1}^{\infty} (\Phi_{\text{ISC}} \Phi_{\text{RISC}})^m \Phi_{\text{p}} \quad (13)$$

$$\text{where } \Phi_{\text{ISC}} = \frac{k_{\text{ISC}}}{k_{\text{T}}^{\text{S}} + k_{\text{nr}}^{\text{S}} + k_{\text{ISC}}} \text{ and } \Phi_{\text{RISC}} = \frac{k_{\text{RISC}}}{k_{\text{T}}^{\text{T}} + k_{\text{ISC}}^0 + k_{\text{RISC}}}.$$

The resultant prompt and delayed fluorescence quantum efficiencies are 54.7 and 43.2%, respectively, at 300 K, and the total photoluminescent efficiency is 97.9%, which is in agreement with the experimental value of  $90 \pm 5\%$  observed in the solid state. As the temperature is decreased, the situation will dramatically change (see Table 3). As can be seen in Table 3, the values of  $k_{\text{T}}^{\text{S}}$  and  $k_{\text{T}}^{\text{T}}$  are expected to hardly change with temperature.  $k_{\text{nr}}^{\text{S}}$  increases with a decrease in the temperature, due to the larger energy gap between  $S_1$  and  $S_0$ , and  $k_{\text{ISC}}$  dramatically increases with increasing temperature. More interestingly, the RISC rate  $k_{\text{RISC}}$  is substantially decreased by 8 orders of magnitude when the temperature is reduced from 300 to 30 K. At a low temperature of  $T = 30$  K,  $k_{\text{RISC}}$  becomes very small, about  $8.59 \times 10^{-3}$   $\text{s}^{-1}$ , while the  $k_{\text{T}}^{\text{T}}$  rate only changes slightly from  $k_{\text{T}}^{\text{T}} = 3.29 \times 10^3$   $\text{s}^{-1}$  to  $3.52 \times 10^3$   $\text{s}^{-1}$ . Moreover, we also found that  $k_{\text{ISC}} = 1.98 \times 10^0$   $\text{s}^{-1}$  is about 7 orders of magnitude smaller than  $k_{\text{T}}^{\text{S}} = 1.22 \times 10^7$   $\text{s}^{-1}$ , which shows that their ratio reaches a level close to this kinetic limit case. Compared with room temperature,  $k_{\text{ISC}} > k_{\text{T}}^{\text{S}} + k_{\text{nr}}^{\text{S}}$  and  $k_{\text{RISC}} > k_{\text{T}}^{\text{T}} + k_{\text{ISC}}^0$ , these limits are not obviously satisfied at low temperatures. The TADF processes do not emerge.

To gain a deep insight into the structure-property relationship during the conversion processes of  $T_1 \leftrightarrow S_1$  and  $S_1 \rightarrow S_0$ , we estimated the Huang-Rhys factor ( $S_i$ ) and the related reorganization energy ( $\lambda$ ) of vibration mode  $i$ , which are shown in Fig. 11 and Fig. S2 (ESI†). We know that the intramolecular reorganization energy,  $\lambda_{\text{intra}}$ , can be represented as a sum of contributions from individual vibrational normal modes  $i$ , as follows:<sup>48</sup>

$$\lambda_{\text{intra}} = \sum \lambda_i = \sum \hbar \omega_i S_i \quad (14)$$

$$S_i = \frac{\omega_i D_i^2}{2\hbar} \quad (15)$$

where  $S_i$ , and  $\omega_i$  represent the Huang-Rhys factor and vibrational frequency for the normal mode  $i$ , respectively;  $D_i$  is the coordinate displacement from the  $T_1$  equilibrium position to the  $S_1$  one along the mode  $i$ . Thus, the Huang-Rhys factor is a useful measure to determine the extent of geometry relaxation between the  $T_1$  and  $S_1$  states. For the conversion between  $T_1$  and  $S_1$ , some low frequency vibration modes ( $< 200$   $\text{cm}^{-1}$ ) have larger  $S_i$ , which correspond to the rotational motion of the phenylene ring of the pop ligand (see Fig. S3, ESI†). This implies that the free rotation of the phenylene ring can provide an important channel to energy conversion between  $T_1$  and  $S_1$ , and the intuitive picture comparing the  $S_1$  and  $T_1$  geometries of Cu(pop)(pz<sub>2</sub>Bph<sub>2</sub>) is shown Fig. S4 (ESI†). In contrast, as with the decay process from  $S_1$  to  $S_0$ , the

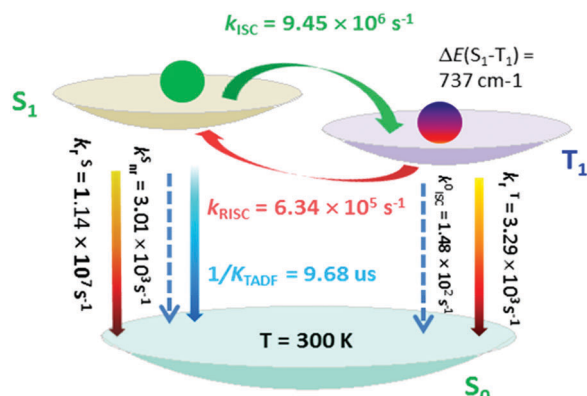


Fig. 10 The calculated conversion and decay rates (in unit of  $\text{s}^{-1}$ ) of the  $S_1$  and  $T_1$  states at 300 K.  $k_{\text{T}}^{\text{S}}$ ,  $k_{\text{T}}^{\text{T}}$ ,  $k_{\text{nr}}^{\text{S}}$ ,  $k_{\text{ISC}}$ , and  $k_{\text{RISC}}$  are the rate constants of fluorescence, phosphorescence, non-radiation, intersystem crossing, and reverse intersystem crossing.

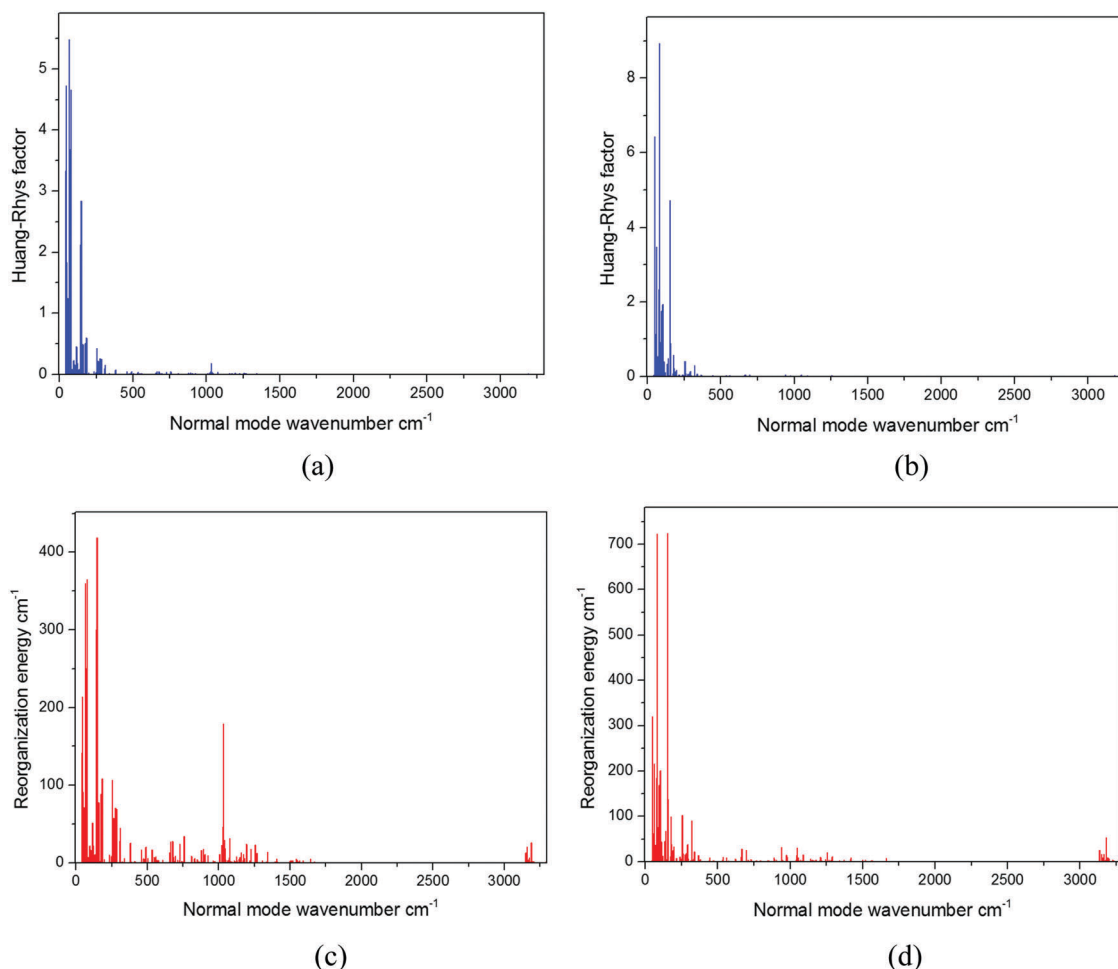


Fig. 11 Calculated Huang–Rhys factors and reorganization energies versus the normal modes in terms of the corresponding  $T_1$  (a and c) and  $S_1$  (b and d) potential surfaces at the PCM-tuned LC-BLYP\* level.

vibration normal modes with a large  $\lambda_{\text{intra}}$  also occur in the high frequency regions,  $500\text{ cm}^{-1}$  to  $1500\text{ cm}^{-1}$  (Fig. S2, ESI†), and they have a reorganization energy,  $\lambda_{\text{intra}}(S_1) \approx 0.47\text{ eV}$ . Therefore, the energy dissipation processes from  $S_1$  to  $S_0$  are much slower than the radiative decay rates.

## Conclusions

In this study, we have quantitatively investigated the geometries and photophysical properties of a TADF Cu(pop)(pz<sub>2</sub>Bph<sub>2</sub>) crystal complex using a methodology proposed by Sun's group. This method is based on the combination of an optimal tuning of the range-separation parameter  $\omega$  in a long-range corrected functional with the PCM-tuned approach, in which the solid-state screening effects are described *via* the consideration of the solid-state dielectric constant  $\epsilon$ . The calculated results have demonstrated that optimising  $\omega$  within the LC-BLYP\* functional provides excellent agreement with the experimental data. For example, compared to the experimental value of  $\Delta E(S_1-T_1) = 800\text{ cm}^{-1}$ , it is apparent that the PCM-tuned ( $\omega = 0.0475\text{ Bohr}^{-1}$ ) LC-BLYP\*/ROCIS ( $737.2\text{ cm}^{-1}$ ) method

gives the best prediction of  $\Delta E(S_1-T_1)$  at the  $T_1$  geometry. As a consequence, the Cu(pop)(pz<sub>2</sub>Bph<sub>2</sub>) complex is a highly attractive candidate for studies and applications of TADF.

Importantly, we know that TADF can effectively take place through the RISC process of  $T_1 \leftrightarrow S_1$ . To ascertainably take place, the  $S_1$  state has to be repopulated with a temperature increase. This signifies that the RISC rate ought to be larger than the rates of the radiative and nonradiative decay of the  $T_1$  state to the ground state. However, the  $S_1$  and  $T_1$  states have the same configurations and their mutual SOC interaction is very weak, and so the vibronic effects may have to be taken into account. In this work, the photophysical properties including the radiative and the nonradiative decay rates arising from SOC of the excited states have been investigated theoretically using the TVCF method. At 300 K, RISC proceeds at a rate of  $k_{\text{RISC}} = 6.34 \times 10^5\text{ s}^{-1}$ , which is 2 orders of magnitude larger than the phosphorescence rate,  $k_{\text{r}}^T = 3.29 \times 10^3\text{ s}^{-1}$ , at the same time,  $k_{\text{RISC}}$  is 3 orders of magnitude larger than the ISC rate of  $k_{\text{ISC}}^0 = 1.48 \times 10^2\text{ s}^{-1}$  from  $T_1$  to  $S_0$ . This means that the  $S_1$  state can be populated from the  $T_1$  state. The delayed fluorescence can occur, where the computed TADF decay time is  $\tau(\text{DF}) = 9.68\text{ }\mu\text{s}$ , the experimental value of which is  $13\text{ }\mu\text{s}$ . The prompt and delayed



fluorescence quantum efficiencies  $\Phi_p$  and  $\Phi_d$  are 54.7 and 43.2%, respectively, and the total photoluminescent efficiency is 97.9%, which is in agreement with the experimental value of  $90 \pm 5\%$  observed in the solid state. At a low temperature  $T < 100$  K, these limits of the TADF process,  $k_{\text{ISC}} > k_r^S + k_{\text{nr}}^S$  and  $k_{\text{RISC}} > k_r^T + k_{\text{ISC}}^0$ , are not obviously satisfied, and therefore, TADF cannot take place.

## Conflicts of interest

There are no conflicts to declare.

## Acknowledgements

The work is supported by the National Natural Science Foundation of China (Grant No. 21263022, 21663025, 21663024). We gratefully thank Dr Haitao Sun (East China Normal University) for providing help in using the PCM-tuned LC-BLYP\* approach.

## References

- H. Xu, R. F. Chen, Q. Sun, W. Lai, Q. Q. Su, W. Huang and X. G. Liu, *Chem. Soc. Rev.*, 2014, **43**, 3259–3302.
- Z. Y. Yang, Z. Mao, Z. L. Xie, Y. Zhang, S. W. Liu, J. Zhao, J. R. Xu, Z. G. Chi and M. P. Aldred, *Chem. Soc. Rev.*, 2017, **46**, 915–1016.
- Y. Tao, K. Yuan, T. Chen, P. Xu, H. H. Li, R. F. Chen, C. Zheng, L. Zhang and W. Huang, *Adv. Mater.*, 2014, **47**, 7931–7956.
- (a) H. Yersin, A. F. Rausch, R. Czerwieniec, T. Hofbeck and T. Fischer, *Coord. Chem. Rev.*, 2011, **255**, 2622–2652; (b) A. F. Rausch, H. H. H. Homeier and H. Yersin, *Top. Organomet. Chem.*, 2010, **29**, 193–235.
- T. Ogiwara, Y. Wakikawa and T. Ikoma, *J. Phys. Chem. A*, 2015, **119**, 3415–3418.
- M. A. Baldo, D. O'brien, Y. You, A. Shoustikov, S. Sibley, M. Thompson and S. Forrest, *Nature*, 1998, **395**, 151–154.
- C. Adachi, *Jpn. J. Appl. Phys.*, 2014, **53**, 060101.
- C. Adachi, M. A. Baldo, M. E. Thompson and S. R. Forrest, *J. Appl. Phys.*, 2001, **90**, 5048–5505.
- B. Zhao, T. Zhang, B. Chu, W. Li, Z. Su, Y. Luo, R. Li, X. Yan, F. Jin and Y. Gao, *Org. Electron.*, 2015, **17**, 15–21.
- H. Uoyama, K. Goushi, K. Shizu, H. Nomura and C. Adachi, *Nature*, 2012, **492**, 234–238.
- T. Chen, L. Zheng, J. Yuan, Z. F. An, R. F. Chen, Y. Tao, H. H. Li, X. J. Xie and W. Huang, *Sci. Rep.*, 2015, **5**, 10923.
- R. Czerwieniec, M. J. Leidl, H. H. H. Homeier and H. Yersin, *Coord. Chem. Rev.*, 2016, **325**, 2–28.
- (a) L. Bergmann, D. M. Zink, S. Bräse, T. Baumann and D. Volz, *Top. Curr. Chem.*, 2016, **374**, 22–39; (b) M. J. Leidl, V. A. Krylova, P. I. Djurovich, M. E. Thompson and H. Yersin, *J. Am. Chem. Soc.*, 2014, **136**, 16032–16038; (c) L. L. Lv, K. Yuan and Y. C. Wang, *Org. Electron.*, 2017, **51**, 207–219; (d) T. Hofbeck, U. Monkowius and H. Yersin, *J. Am. Chem. Soc.*, 2015, **137**, 399–404; (e) L. L. Lv, K. Yuan and Y. C. Wang, *Org. Electron.*, 2018, **52**, 110–122.
- R. Czerwieniec, J. Yu and H. Yersin, *Inorg. Chem.*, 2011, **50**, 8293–8301.
- J. Föller, M. Kleinschmidt and C. M. Marian, *Inorg. Chem.*, 2016, **55**, 7506–7516.
- F. B. Dias, K. B. Bourdakos, V. Jankus, K. C. Moss, K. T. Kamtekar, V. Bhalla, J. Santos, M. R. Bryce and A. P. Monkman, *Adv. Mater.*, 2013, **25**, 3707–3714.
- J. Gibson, A. P. Monkman and T. J. Penfold, *ChemPhysChem*, 2016, **17**, 2956–2961.
- (a) H. T. Sun, C. Zhong and J.-L. Brédas, *J. Chem. Theory Comput.*, 2015, **11**, 3851–3858; (b) H. T. Sun, S. Ryno, C. Zhong, M. K. Ravva, Z. R. Sun, T. Körzdörfer and J.-L. Brédas, *J. Chem. Theory Comput.*, 2016, **12**, 2906–2916; (c) H. T. Sun, C. Zhong and Z. R. Sun, *Acta Phys.-Chim. Sin.*, 2016, **32**, 2197–2208; (d) H. T. Sun, Z. B. Hu, C. Zhong, X. K. Chen, Z. R. Sun and J.-L. Brédas, *J. Phys. Chem. Lett.*, 2017, **8**, 2393–2398.
- (a) Q. Peng, Y. P. Yi, Z. G. Shuai and J. S. Shao, *J. Chem. Phys.*, 2007, **126**, 114302; (b) Q. Peng, Y. Yi, Z. G. Shuai and J. S. Shao, *J. Am. Chem. Soc.*, 2007, **129**, 9333–9339.
- Y. L. Niu, Q. Peng, C. M. Deng, X. Gao and Z. G. Shuai, *J. Phys. Chem. A*, 2010, **114**, 7817–7831.
- Q. Peng, Y. L. Niu, Q. Shi, X. Gao and Z. G. Shuai, *J. Chem. Theory Comput.*, 2013, **9**, 1132–1143.
- Q. Peng, Q. H. Shui, Y. L. Niu, Y. P. Yi, S. R. Sun, W. Q. Li and Z. G. Shuai, *J. Mater. Chem. C*, 2016, **4**, 6829–6838.
- M. Roemelt and F. Neese, *J. Phys. Chem. A*, 2013, **117**, 3069–3083.
- A. M. Dreuw and M. Head-Gordon, *J. Am. Chem. Soc.*, 2004, **126**, 4007–4016.
- J. Autschbach and M. Srebro, *Acc. Chem. Res.*, 2014, **47**, 2592–25602.
- D. J. Tozer, *J. Chem. Phys.*, 2003, **119**, 12697–12699.
- T. Körzdörfer and J. L. Brédas, *Acc. Chem. Res.*, 2014, **47**, 3284–3291.
- S. P. Huang, Q. S. Zhang, Y. Shiota, T. Nakagawa, K. Kuwabara, K. Yoshizawa and C. Adachi, *J. Chem. Theory Comput.*, 2013, **9**, 3872–3877.
- U. Salzner and A. Aydin, *J. Chem. Theory Comput.*, 2011, **7**, 2568–2583.
- T. Stein, L. Kronik and R. Baer, *J. Am. Chem. Soc.*, 2009, **131**, 2818–2820.
- T. Yanai, D. P. Tew and N. C. Handy, *Chem. Phys. Lett.*, 2004, **393**, 51–57.
- J. Tomasi, B. Mennucci and R. Cammi, *Chem. Rev.*, 2005, **105**, 2999–3094.
- Z. Hu, B. Zhou, Z. Sun and H. Sun, *J. Comput. Chem.*, 2017, **38**, 569–575.
- T. Lu, *optDFTw and scanDFTw programv1.0*, <http://sobereva.com/346>, 2017.3.8.
- A. V. Kityk, *J. Phys. Chem. A*, 2012, **116**, 3048–3055.
- M. J. Frisch, G. W. Trucks and H. B. Schlegel *et al.*, *Gaussian 09, Revision-D.01*, Gaussian Inc., Wallingford, CT, 2009.
- F. Neese, The ORCA program system, *WIREs Comput. Mol. Sci.*, 2012, **2**, 73–78.
- M. Roemelt, D. Maganas, S. DeBeer and F. Neese, *J. Chem. Phys.*, 2013, **138**, 204101.

- 39 B. Sandhoefer and F. Neese, *J. Chem. Phys.*, 2012, **137**, 094102.
- 40 F. Neese, F. Wennmohs, A. Hansen and U. Becker, *Chem. Phys.*, 2009, **356**, 98–109.
- 41 F. Neese, *J. Chem. Phys.*, 2005, **122**, 034107.
- 42 B. Minaev, G. Baryshnikov and H. Ågren, *Phys. Chem. Chem. Phys.*, 2016, **16**, 1719–1758.
- 43 G. Baryshnikov, B. Minaev and H. Ågren, *Chem. Rev.*, 2017, **117**, 6500–6537.
- 44 Q. Peng, D. Fan, R. H. Duan, Y. P. Yi, Y. L. Niu, D. Wang and Z. G. Shuai, *J. Phys. Chem. C*, 2017, **121**, 13448–13456.
- 45 M. Tanabe, H. Matsuoka, Y. Ohba, S. Yamauchi, S. Yamauchi, K. Sugisaki, K. Toyota, K. Sato, T. Takui, I. Goldberg, I. Saltsman and Z. Gross, *J. Phys. Chem. A*, 2012, **116**, 9662–9673.
- 46 R. Czerwieniec and H. Yersin, *Inorg. Chem.*, 2015, **54**, 4322–4327.
- 47 F. B. Dias, T. J. Penfold and A. P. Monkman, *Methods Appl. Fluoresc.*, 2017, **5**, 012001.
- 48 P. K. Samanta, D. Kim, V. Coropceanu and J.-L. Brédas, *J. Am. Chem. Soc.*, 2017, **139**, 4042–4051.